Transient electroluminescence of polymer light emitting diodes using electrical pulses

D. J. Pinner, R. H. Friend, and N. Tessler[a)]

Cavendish Laboratory, Madingley Road, Cambridge CB3 0HE, United Kingdom

Detailed experimental and theoretical analysis of the pulsed excitation of polymer light emitting diodes is presented. We find a set of universal transient features for a variety of device configurations (different polymers/cathodes) which can be reproduced using our phenomenological numerical model. We find that the temporal evolution of the electroluminescence in response to a step voltage pulse is characterized by: (i) a delay followed by; (ii) a fast initial rise at turn-on followed by; (iii) a slow rise (slower by at least one order of magnitude). The large mobility mismatch between holes and electrons in conjugated polymers allows us to separately time resolve the motion of holes and electrons. We suggest a method for extracting mobility values that takes into account the possible field-induced broadening of carrier fronts, and which is found to be compatible with mobilities determined from constant wave measurements. By using appropriate device configurations it is possible to determine the mobilities of both holes and electrons from a single device. Mobilities for holes and electrons are extracted for a poly(*p*-phenylenevinylene) copolymer and poly(di-octyl fluorene). © *1999 American Institute of Physics.* [S0021-8979(99)07621-5]

I. INTRODUCTION

The pulsed electrical excitation of polymer light emitting diodes (LEDs) has been widely reported upon[1–10] since measurements of transient electroluminescence (EL) provide information on charge transport processes in the device. Short duration, low duty-cycle electrical pulses minimize the Joule heating effects[6–11] often associated with device failure in constant wave (CW) conditions, and allow access to higher field regimes ($>10^7$ V cm^{-1}).[6,7] The high peak brightnesses ($5–20\times10^6$ cd m^{-2}),[12] peak current densities (kA cm^{-2}),[7,13] and fast EL modulation achieved under pulsed operation also show promise for the future realization of polymer laser diodes and multiplexed displays.

There is, however, a need for systematic experimental studies using electrical pulses due to the complicated interplay of injection, space charge build up, charge transport, recombination, and extrinsic heating effects in the device. Moreover, mobility values obtained using pulsed measurements have been found inconsistent with the interpretation of CW current density–voltage ($J-V$) measurements and/or time of flight (TOF) techniques.[9] In this article we examine the experimental procedure for time-resolved pulsed measurements of LEDs and compare it to CW operation. Using a phenomenological model we provide a framework for the interpretation of pulsed data. Our method relies on several features of the transient EL, which we find to be general to a wide variety of systems (single, double layer devices, different polymers, and different cathodes). In particular, we find two distinct components in the EL turn-on, after the application of a step voltage, which we attribute to the motion of different charge carriers species (electrons and holes). The time-resolved method is used to determine both the hole mobility, μ_h, and the electron mobility, μ_e, for two different polymers as a function of the applied voltage.

II. EXPERIMENT

A. Device fabrication

The LEDs investigated were fabricated on indium tin oxide (ITO) coated glass substrates as the hole-injecting electrode. The ITO substrates were metallized with 100-nm-thick aluminum strips (covered with an insulating layer of aluminum oxide) to reduce the resistance of the ITO sheet between the pulse generator and the active area, as reported in Ref. 13, and plasma etched to improve hole injection.[14] The active area of the diodes was 1 mm^2 and the residual resistance was less than 3 Ω. The polymers used in the devices were: doped polyethylene dioxythiophene/polystyrene sulphonate (PEDOT:PSS)[15,16] (used as an anode layer); poly(*p*-phenylenevinylene) (PPV); a copolymer of PPV consisting of conjugated PPV segments and nonconjugated acetylene-*p*-xylylene units (PPV copolymer)[13,15] (see Fig. 3), and poly(di-octyl fluorene) (PFO) (see Fig. 8). The PFO had a molecular weight, M_w, of $\sim$90 000 and was prepared as a 1.6% weight per volume of solution in mixed xylenes.

The five LEDs structures investigated were: device A [ITO/PPV (220 nm)/Ag]; device B [ITO/PPV (220 nm)/Au]; device C [ITO/PEDOT:PSS (50 nm)/PPV copolymer (75 nm)/Ca]; device D [ITO/PFO (100 nm)/Ca]; and device E [ITO/PEDOT:PSS (50 nm)/PFO (75 nm)/Ca] (see Table I). For devices C and E the water-soluble PEDOT:PSS layer was spun in air and baked in nitrogen at 200 °C for 1 h. All further fabrication processes (spin casting, thermal conversion, contact evaporation) were performed in a nitrogen glove box. The remaining devices were fabricated entirely in the nitrogen glove box. The fabrication procedure of the devices was consistent with devices that have previously

[a)]Present address: EE Dept., Technion, Haifa 32000, Israel; electronic mail: nir@ee.technion.ac.il

TABLE I. Summary of the injection characteristics of devices A–E and of the specific design purposes of the devices.

Device	Device structure	Δ_e (eV)	$\Delta_{h\text{MAX}}$ (eV)	Electron-injection limited?	Hole-injection limited?	Design purpose
A	ITO/PPV/Ag	~1.8	~0.3	Yes	No	(1) Transient EL features in electron-injection-limited system
B	ITO/PPV/Au	~2.4	~0.3	Yes	No	(1) Low voltage J–V (~flat band at $V=0$ V)
C	ITO/PPV copolymer/Ca	~0.2	~0.2	No	No	(1) CW vs pulsed J–V (current heating effects) (2) Extracting μ_h (& μ_e at low V)
D	ITO/PFO/Ca	~0.1	~1.0	No	Yes	(1) Transient EL features in hole-injection-limited system (2) Extracting μ_e & μ_h
E	ITO/PEDOT:PSS/ PFO/Ca	~0.1	~0.9	No	Yes	(1) Charge storage effects of PEDOT:PSS layer

shown good performances. For example, structures similar to device C, using the PPV copolymer, have previously produced peak brightnesses of $5-20\times10^6$ cd m^{-2}.[7,12,13]

The PPV films were prepared by thermal conversion of the spun precursor polymer film in a dynamic vacuum of 10^{-5} mbar with an inert base atmosphere. Several authors[17–19] have addressed the problem of PPV doping from the ITO during thermal conversion. To minimize this effect the PPV was converted by ramping up the temperature slowly (1 °C min^{-1}) from room temperature to 250 °C. This temperature of 250 °C was then maintained for 10 h before allowing the sample to cool under vacuum. The slow ramp rate serves both to reduce the interaction effects of trapped chlorine with the ITO and to improve conversion uniformity throughout the film. The PPV copolymer was prepared via a similar precursor polymer route using a conversion temperature of 200 °C for 4 h.[13] It has been shown[20] that PPV can be chemically doped by PEDOT:PSS when converted on top of the PEDOT:PSS layer from the PPV precursor. For this work, however, the PEDOT:PSS was used in conjunction with a different PPV (requiring different conversion conditions), and no evidence of chemical doping was found during device testing.

Figure 1 shows the current density, J, plotted versus the applied voltage, V, on a double logarithmic scale for device B [ITO/PPV (220 nm)/Au] for voltages from 0.01 to 2 V. We can clearly identify two types of current-density behavior from the plot, namely: (i) ohmic, $J \propto V$, for $V < 0.4$ V and (ii) space charge limited current (SCLC), $J \propto V^2$ for 0.4 V $< V < 2$ V. The equations defining ohmic and SCLC behavior, respectively, are

$$J_{\text{ohmic}} = n_0 q \mu_{\text{eff}} \frac{V}{L} \tag{1}$$

$$J_{\text{SCLC}} = \frac{9}{8} \epsilon_r \epsilon_0 \mu_{\text{eff}} \frac{V^2}{L^3}, \tag{2}$$

where n_0 is the extrinsic carrier density (i.e., the density of noninjected charge present in the PPV film), q is the elec-

tronic charge, μ_{eff} is the effective mobility[21] which for $\mu_h \gg \mu_e$ reduces to $\mu_{\text{eff}} \cong \mu_h$, L is the device thickness, ϵ_0 is the permitivity of free space, and ϵ_r is the relative permitivity of the polymer. Assuming that the ohmic and SCLC descriptions are valid for this system, these equations may then be used to calculate n_0 and μ_{eff} from the current-density, J_Ω, and the voltage, V_Ω, at the crossover from ohmic to SCLC behavior (see Fig. 1). These are measured here by the intersection of the first and second gradients fitted to the lower and higher voltage regimes respectively, as shown in Fig. 1. (The V^2 regime has previously been shown to extend to higher voltages before the field dependent mobility start to significantly influence J).[22] Neglecting the built-in voltage, V_{bi}, between ITO and gold, and using Fig. 1 we find that $V_\Omega = 0.4$ V. Since for most organic materials the hole mobility, μ_h, is found to be much greater than the electron mobility, μ_e, we may assume that $\mu_{\text{eff}} \cong \mu_h (\mu_h \gg \mu_e)$, Eqs. (1) and (2), allow us to calculate the hole mobility for the polymer (this assumption is justified later in the article). In this manner (and assuming $\epsilon_r = 3$ for PPV) we estimate the density of extrinsic charge, n_0, in the PPV film of device B
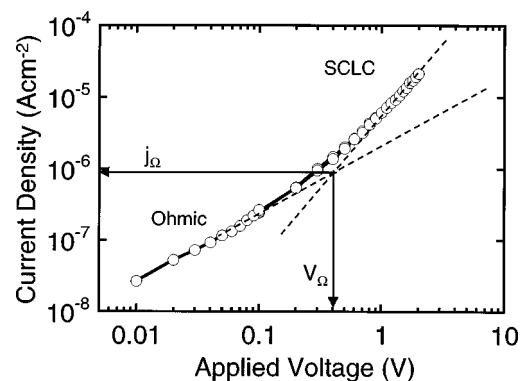

FIG. 1. Current density as a function of the applied voltage for device B [ITO/PPV (200 nm/Au] for the voltage range 0.01–2 V. J_Ω and V_Ω are the current density and voltage (respectively) at the crossover from ohmic ($J \propto V$) to SCLC ($J \propto V^2$) behavior.

upon completion of all processing steps to be $\sim 1.4 \times 10^{15}\,\text{cm}^{-3}$, and the hole mobility, μ_h, to be $\sim 2 \times 10^{-7}\,\text{cm}^2\,\text{V}^{-1}\,\text{s}^{-1}$ for electric fields in the range between 500 V cm^{-1} and 0.1 MV cm^{-1}.

A similar procedure can be performed from the $J-V$ curve (not shown) for device A [ITO/PPV (220 nm)/Ag] from which we calculate $n_0 \sim 4 \times 10^{14}\,\text{cm}^{-3}$ and $\mu_h \sim 1.4 \times 10^{-6}\,\text{cm}^{-2}\,\text{V}^{-1}\,\text{s}^{-1}$, these values being approximately three times smaller and seven times bigger than those of device B, respectively. It is likely that these differences are an indication of the errors in either V_{bi} or V_{Ω}, rather than of the different systems' individual properties. We may therefore conclude that for our PPV LEDs we have $n_0 < 10^{15}\,\text{cm}^{-3}$ and $\mu_h \sim 10^{-7}-10^{-6}\,\text{cm}^2\,\text{V}^{-1}\,\text{s}^{-1}$. These levels of background charge are one to two orders of magnitude lower than those values quoted in the literature for thermally converted PPV on ITO.[1,18] Moreover, in a device structure such as ITO/PPV/Au, the bands are almost flat at zero bias. Equilibrium between the contacts and the polymer will result in charge diffusion into the polymer and an apparent doping effect. Assuming a density of states of $10^{21}\,\text{cm}^{-3}$ the charge concentrations at the interface for metal/polymer injection barriers $(\Delta\phi)$ of 0.2 and 0.3 eV are $[P_0 = 10^{21} \times \exp(-\Delta\phi/KT)] \sim 10^{17}$ and $10^{16}\,\text{cm}^{-3}$, respectively. This suggests that $10^{15}\,\text{cm}^{-3}$ is probably an upper limit for chemical doping. We attribute these low background charge levels to both the device fabrication technique and the careful synthesis of the PPV precursor.

B. Electrical excitation of LEDs

The LEDs were electrically excited by means of a homemade pulse generator with a 10 ns rise time and operating frequencies from 10 mHz to 100 kHz. Unless explicitly stated the repeat frequency used was 1 Hz. The voltage drop across the LED was measured with a voltage probe ($\sim$10 ns rise time) and the current was monitored with an induction current probe[23] ($\sim$5 ns rise time). The temporal evolution of the light output was measured using a photomultiplier tube (PMT) with a 50 ns delay time and a 15 ns rise time. The overall response time of the system is 15–20 ns. Voltage, current, and light signals were measured using a Hewlett Packard 400 MHz bandwidth digitizing oscilloscope (HP 54502A). CW current voltage characteristics were measured using the Keithley 230 and Keithley 195, respectively.

C. Device design

Figure 2 shows a schematic of the band diagrams for the five devices investigated, showing the relevant levels for the injection and transport of carriers. The values for the highest occupied molecular orbital (HOMO) and the lowest unoccupied molecular orbital (LUMO) were estimated from cyclic voltametry measurements, Kelvin probe measurements, and from the literature.[24] The metal workfunctions, φ_m, are from[25] and the workfunction of plasma etched ITO, φ_{ITO}, is from Ref. 14. The barrier to electron injection, Δ_e, and the largest barrier to hole injection, $\Delta_{h\text{MAX}}$, (between the etched ITO and the emitter interface) are annotated on the band diagram for device A, and listed for all five devices in Table
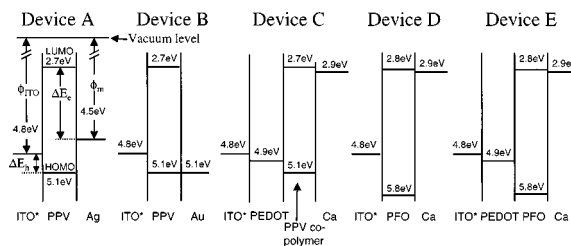

FIG. 2. Schematic representation of the band diagrams for devices A–E. Shown relative to the vacuum level for device A are the work function of ITO, ϕ_{ITO}, the work function of the metal cathode, ϕ_m, the HOMO of the polymer, the LUMO of the polymer, the maximum energy barrier to hole injection between the ITO and the emitting polymer, $\Delta_{h\text{MAX}}$ and the energy barrier to electron injection, Δ_c. The values for the injection energy barriers are listed in Table I.

I. It should be noted that the interaction between the polymer and the electrodes may result in smaller barrier heights for electron injection and larger values for hole injection than quoted here.[26–28] However, the analysis presented later does not depend on these values being accurate.

It has been postulated that the current density is injection limited if the injection barrier is larger than 0.3–0.4 eV.[29,30] Using this criterion devices A and B are electron-injection limited, device C is neither electron nor hole-injection limited, and devices D and E are hole-injection limited. Table I also shows how the different properties of the polymers and electrodes were used to design devices for specific purposes. In particular, the device designs make use of the different combinations of Δ_e and $\Delta_{h\text{ MAX}}$ to facilitate or inhibit the injection of particular carriers.

Since for most organic materials $\mu_h \gg \mu_e$, it is generally considered that in structures such as these five devices the holes will be transported faster than electrons under an applied electric field once they have been successfully injected. For devices that are not hole-injection limited (devices A, B, and C) the average hole density will be much greater than the electron density, such that hole transport dominates the $J-V$ characteristics. In this case the recombination zone is initially located close to the cathode. For cases where the device is hole-injection limited but not electron-injection limited (devices D and E), the average electron density will be much greater than the average hole density, but the electron mobility remains much smaller than the hole mobility. The combination of these mismatches makes the carrier dynamics of the hole-injection limited device more complicated than that of the electron injection limited device.

We will later use device C, which is neither hole- nor electron-injection limited, to measure the hole mobility (and the electron mobility in the low field regime) of the PPV copolymer. The high current densities achieved in device C preclude us from extracting the electron mobility in the high field regime due to heating effects. Similarly, device D (hole-injection limited) will be used to measure both the electron and hole mobility of PFO. The low light levels produced from the highly electron-injection-limited devices A and B, however, make these devices unsuitable for hole mobility determination, as the voltages required to produce measurable light are so large as to make the EL response time reso-
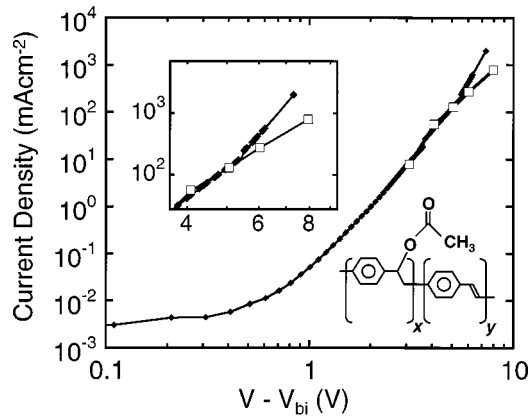
FIG. 3. Current density as a function of the applied voltage minus the built-in voltage for device C [ITO/PEDOT (50 nm)/PPV copolymer (75 nm)/Ca] in both CW (filled diamonds) and pulsed (empty squares) modes. The inset shows detail of the region where the CW and pulsed mode current densities diverge. The structure of the PPV copolymer is also shown.

FIG. 4. Numerical simulation of the current density as a function of voltage for a 1 mm^2 device in the CW drive scheme by taking into consideration current-induced heating effects. The full line is calculated for $R_T = 0$ K/W, the dashed-dotted line for $R_T = 160$ K/W, and the dashed line for $R_T = 1600$ K/W. The bottom curve shows the calculated current density for $T_{HS} = 200$ K.

lution limited. As discussed earlier, device B was designed to obtain reliable low voltage $J-V$ characteristics by virtue of its low built-in voltage. Finally, device F was designed to investigate the effect of the inclusion of the PEDOT:PSS anode layer on the charge storage effects of the ITO/PFO/Ca system.

D. Current heating effects

1. CW versus pulsed J–V characteristics

At the low voltages and current densities shown in Fig. 1, the effects of heating due to the dissipated power in the device are negligible. This may no longer hold at high volt-
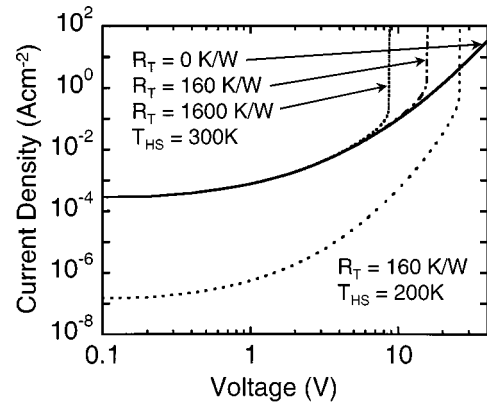
ages when the current densities become much larger. CW measurements therefore have the inherent problem that the device temperature increases even whilst the voltage is held constant during a typical CW $J-V$ measurement because of Joule heating.[6] It is known that for a given voltage, the current increases with increasing temperature (attributed to enhanced thermally assisted hopping).[22,31–37] Figure 3 shows the current density as a function of the applied voltage minus the built-in voltage ($V-V_{bi}$) for device C in both CW and pulsed mode. A 10 Hz repetition frequency was used for the pulsed measurements and the current densities were read from the quasisteady-state region of the pulse. We see that at

TABLE II. Summary of the parameter values used in the phenomenological simulation model for a PPV-like polymer device similar to device C (col. 2), and a PFO polymer device similar to device D (col. 3).

Quantity	Parameters used for PPV-like polymer device	Parameters used for PFO-like polymer device
Device thickness, z	100 nm	75 nm
Device area, A	1 mm^2	1 mm^2
Electron injection barrier, Δ_e	0.2 eV	0.1 eV
Hole injection barrier, Δ_h	0.3 eV	1.0 eV
Hole mobility, μ_h	$\mu_h = \mu_{h,0} e^{-\Delta/kT} e^{\gamma\sqrt{E}}$ (Ref. 9)	$\mu_h = 10^{-4}$ cm^2 V^{-1} s^{-1} (from Sec. VI A)
Electron mobility, μ_e	$\mu_e = 0.1\mu_h$ (assumption)	$\mu_e = \mu_{e,0} e^{-\Delta/kT} e^{\gamma\sqrt{E}}$
Zero field mobility, μ_0	$\mu_{h,0} = 35$ cm^2 V^{-1} s^{-1} (Ref. 9) $\mu_{h,0} e^{-\Delta/kT} = 3.4\times10^{-7}$ cm^2 V^{-1} s^{-1}	$\mu_{e,0} e^{-\Delta/kT} = 7.5\times10^{-10}$ cm^2 V^{-1} s^{-1} (from Sec. VI B)
Thermal activation energy, Δ	0.48 eV (Ref. 9)	⋯
B	2.9×10^{-5} eV (Ref. 9)	⋯
T_0	600 K (Ref. 9)	⋯
T	300 K	300 K
γ	5.6×10^{-3} cm$^{1/2}$ V$^{-1/2}$ (Ref. 9)	4.4×10^{-3} cm$^{1/2}$ V$^{-1/2}$ (from Sec. VI B)
Relative permittivity of polymer, ϵ_r	3	
Fraction of excitons formed as singlets, F	1/4	
Exciton lifetime, τ	1 ns	
Exciton diffusion length, L_D	10 nm (Ref. 46)	
Exciton diffusion coefficient, D	$D = 10^{-3}$ cm^2 s^{-1} (given by $D = L_D^2/\tau$)	
DOS, N_0	N_0 = density of conjugated units = 10^{21} cm^{-3} (Ref. 37)	
Richardson constant, A	120 A cm^{-2} K^{-2} (Ref. 57)	

low voltages there is a good agreement between pulsed and CW data, and that at $\sim V-V_{bi}=6\,\mathrm{V}$ (corresponding to $V=7.9\,\mathrm{V}$ and $J\cong 50\,\mathrm{mA\,cm^{-2}}$, assuming that $V_{bi}\cong 1.9\,\mathrm{V}$)[38] the CW measured current starts to increase faster than the pulsed current (see inset). The ratio of the CW current density, j_{CW}, to the pulsed current density, j_{pulsed}, at the highest CW voltage applied here $(V-V_{bi}=7.2\,\mathrm{V})$ is given by $J_{CW}/J_{pulsed}=3$.

2. Numerical simulation of current heating

To test if heating is a plausible explanation for the differences seen between CW and pulsed $J-V$ measurements we have numerically simulated the $J-V$ behavior by analyzing the commonly used equations assuming (i) a space charge limited current,[39] (ii) single carrier transport, and (iii) a field and temperature dependent mobility, μ.[22] To make our simulation more realistic we add an equation describing current-induced heating[6] for the CW drive scheme. The equations are

$$J=\frac{9}{8}\,\epsilon_r\epsilon_0\mu V^2 L^{-3}\quad (\mathrm{A\,cm^{-2}}) \tag{3}$$

$$\mu=\mu_0\exp\left(-\frac{\Delta}{kT}\right)\exp(\gamma\sqrt{E})\quad (\mathrm{cm^2\,V^{-1}\,s^{-1}}) \tag{4}$$

$$\gamma=B\left(\frac{1}{kT}-\frac{1}{kT_0}\right)\quad (\mathrm{V^{-1/2}\,cm^{1/2}}) \tag{5}$$

$$T=T_{HS}+IVR_T\quad (\mathrm{K}). \tag{6}$$

Here μ_0 is the zero-field mobility, E is the electric field, T is the device temperature, T_{HS} is the heat sink temperature, I is the current, and R_T is the thermal resistance. Table II lists the values used for the parameters, μ_0, Δ, B, and T_0, which were taken from the work done by Blom and Vissenberg on PPV diodes.[9]

Figure 4 shows the $J-V$ characteristic derived by solving Eqs. (3)–(6) self-consistently for a 1 $\mathrm{mm^2}$ device. The full line is calculated for $R_T=0\,\mathrm{K/W}$, the dashed-dotted line for $R_T=160\,\mathrm{K/W}$, and the dashed line for $R_T=1600\,\mathrm{K/W}$. For completeness we have also included a calculation for $T_{HS}=200\,\mathrm{K}$ (bottom curve). $R_T=160\,\mathrm{K/W}$ was calculated for a relatively good heat sinking procedure.[6] Since the resistance of a 1 $\mathrm{mm^3}$ volume of glass is $R_T=110\,\mathrm{K/W}$ values exceeding 1000 K/W may be encountered. Moreover, it was found for CW drive,[41] that the temperature is not uniform even in a 1 $\mathrm{mm^2}$ device, the center of the pixel being hotter than the edges. We note from Fig. 4 that when the device is not properly heat sinked, there is a specific current density $(100-1000\ \mathrm{mA\,cm^{-2}})$ beyond which the current-induced heating raises the device temperature, which in turn enhances both the mobility and current. In this manner a positive feedback loop is established, and the current starts to increase steeply. In a real device one would not expect the current to increase so abruptly, but rather to become limited by other factors (e.g., contacts). We therefore suggest that the difference in slopes and magnitudes described in Fig. 3 is largely attributed to heating under CW drive conditions. Using the temperature dependence of the mobility shown above, the ~ 3 times increase seen in the CW current of device C (Fig.
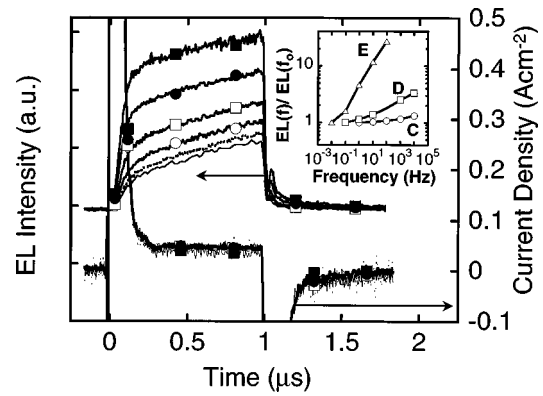

FIG. 5. EL and current-density response of device D to 10 V 1 μs pulses of varying repetition frequency. Repetition frequencies are: 100 mHz (solid line); 1 (dashed line); 10 (open circles); 100 Hz (open squares); 1 (filled circles), and 10 kHz (filled square). The inset shows the amplification of the EL as a function of the repetition frequency for devices C, D, and E.

3) would correspond to a temperature rise of $\sim 20\,\mathrm{K}$. Based on the earlier studies we have used pulsed-mode measurements for the analysis of $J-V$ data.

E. Charge storage between pulses

The presence of charge storage effects in polymer LEDs must be taken into account when performing pulsed measurements, as it is important not to use pulse repetition frequencies that cause significant interference effects between successive pulses. We find that charge storage effects within a device may be easily investigated by the variation of the repetition frequency. In LEDs which have been prepared as described in Sec. II A, one does not expect a predominance of real traps (e.g., induced by oxygen, metal diffusion, doping of PPV from thermal conversion on ITO). The tail of the gaussian density of states (DOS), however, may cause effects similar to traps, something which has been considered by several authors.[26,31,37,42,43] Moreover, the presence of interfacial layers at the electrodes, and between polymer layers may enhance the storage of charge in the device.[44]

Figure 5 shows the EL response as a function of the pulse repetition frequency, f, for device D using 10 V 1 μs pulses. We see that there is a threshold repetition frequency, f_0, above which the integrated EL intensity of a given pulse is seen to rise. For devices C, D, and E, f_0 is found to be $\sim 100\,\mathrm{Hz}$, $\sim 100\,\mathrm{mHz}$, and $<10\,\mathrm{mHz}$, respectively. This implies that the charge ''memory'' effects in devices C, D, and E are ~ 0.01, >10 and >100 s for fields of 0.4, 1.0, and 0.6 $\mathrm{MV\,cm^{-1}}$, respectively. In accord with these findings, the inset of Fig. 5 shows the EL within a given pulse as a function of repetition frequency, $EL(f)$, normalized to the EL at the threshold repetition frequency, $EL(f_0)$. We see that device E is the most frequency sensitive, with $EL(f)/EL(f_0)$ ~ 30 for $f=100\,\mathrm{Hz}$, and that device C is least frequency sensitive with $EL(f)/EL(f_0)\sim 1.3$ for $f=10\,\mathrm{kHz}$. Comparison of the EL responses of devices D and E shows that the inclusion of the PEDOT:PSS anodic polymer layer is responsible for the increased charge storage effects seen for device E. This is probably because the PEDOT:PSS layer is serving
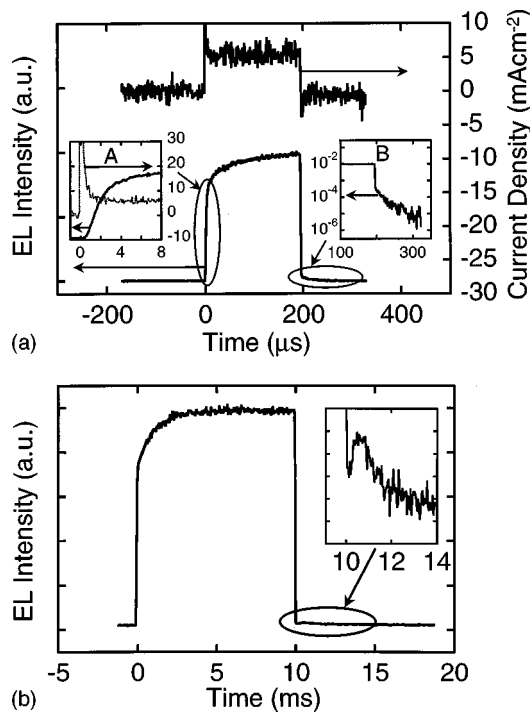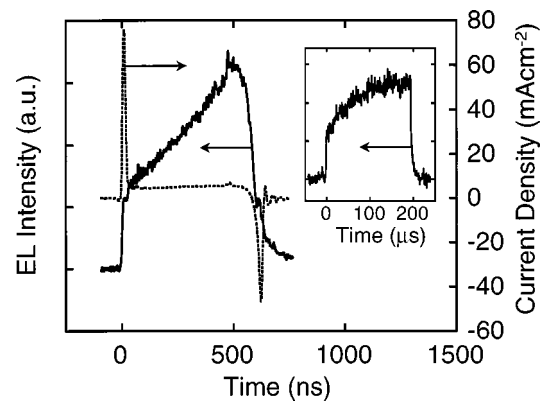
FIG. 7. EL and current-density response of device A to 41 V 600 ns pulses. The inset shows the EL response of the same device to 25 V 200 μs pulses.

FIG. 6. (a) EL and current-density response of device C to 5 V 200 μs pulses. Inset A shows detail of the EL turn-on period and the current charging spike. The delay time, t_d, is the delay between the application of the voltage pulse (corresponding to the onset of the current spike) and the onset of EL ($t_d \sim 750$ ns). Inset A also shows the fast rise time, $t_1 \sim 4.76$ μs. Inset B shows the detail of EL at turn-off on a logarithmic scale showing the fast modulation ($t_3 < 15$ ns) of the EL when the step voltage is removed, and the exponential EL decay of characteristic time, $t_4 \sim 70$ μs. (b) EL response of device C to 5 V 10 ms pulses showing the second and slower rise time in the EL, $t_2 \sim 5$ ms. The inset shows detail of an EL ''satellite'' ~ 0.5 ms after turn-off.

as an electron blocker. This shows that the PEDOT:PSS layer should not purely be though of as a conducting anode. Note that elsewhere in this article we use repetition frequencies which are sufficiently low to avoid interference effects between pulses.

III. TRANSIENT RESPONSE OF LEDS

We now consider the transient response of the LED devices under pulsed operation, with the aim of extracting the charge transport properties and comparing them to the $J-V$ characteristics. We start by carefully examining the experimental procedure using a range of experimental conditions as well as device configurations. By identifying universal features we are able to draw guidelines for the determination of parameters.

A. Transient features: Device C

Figure 6(a) shows the EL and current response for device C to 200 μs 5 V pulses. As discussed earlier this is a PPV copolymer device with the injection of both charge carriers being bulk limited. The EL time evolution is characterized by the following five features listed here in chronological order: (i) a delay time, t_d, before light is detected; (ii) a fast initial rise time, t_1, at EL turn-on; (iii) a second slower rise time, t_2; (iv) fast turn-off modulation (of characteristic

time t_3) to a nonzero EL value followed by (v) a long-lived exponential tail (of characteristic time t_4). The times t_d, t_1, and t_2 will be interpreted and defined in Sec. V when we present the phenomenological simulation model used for this work. Inset A of Fig. 6(a) shows detail of the turn-on period from which we can resolve both t_d and t_1. Inset B of Fig. 6(a) shows detail of the turn-off period. Being of order 15 ns, t_3, we consider that this is limited by the response of the PMT. Plotted on a logarithmic scale we see that after a fast modulation of the EL, for times less than 100 μs, the time constant t_4 of the EL decay can be fitted to a single exponential. Figure 6(b) shows the EL response of device C to 10 ms pulses at 5 V, from which we see that the time scale of the second EL rise is several orders of magnitude longer than that of the first EL rise. The inset of Fig. 6(b), however, shows that on longer time scales there is a further feature or ''bump'' occurring approximately 500 μs after turn-off, followed by a further decay.

For device C at 5 V the delay time, t_d, is ~ 750 ns, the fast and slow rise times are $t_1 \sim 4.75$ μs [inset of Fig. 6(a)] and $t_2 \sim 5$ ms [Fig. 6(b)], respectively. At voltage turn-off the EL drops to $\sim 1/30$ of its previous value [inset B of Fig. 6(a)] within 15 ns and then exponentially decays with a time constant $t_4 \sim 20$ μs. The bump then occurs at ~ 500 μs and decays with a time constant of ~ 200 μs. Experiments show that the bump is only present if the product of the voltage and pulse width is above a certain threshold value suggesting that there is a threshold charge density necessary to produce this feature. We propose an explanation for this feature in Sec. V C. The transient response of the current density is characterized by a sharp charging spike (due to the capacitance of the device) followed by a quasisteady state of ~ 13 mA cm^{-2}. At turn-off there is a sharp discharging spike followed by a long-lived decay.

B. Universality of transient features

To illustrate that the transient EL features discussed so far are general to other systems Fig. 7 shows the transient EL and current density of device A [ITO/PPV (200 nm)/Ag] under 600 ns 41 V pulses, and the inset shows the EL from 200 μs 25 V pulses. Figure 8 shows the transient EL and current density of device D [ITO/PFO (100 nm)/Ca] under
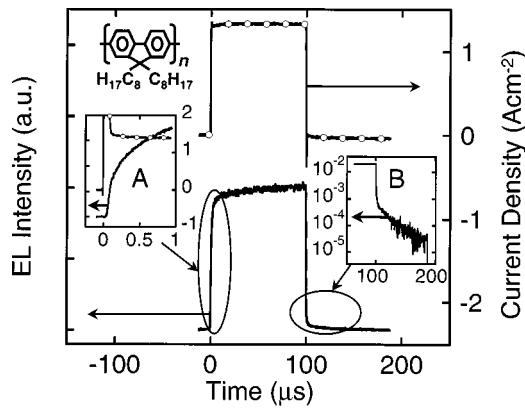
FIG. 8. EL and current-density response of device D to 16 V 100 μs pulses. Inset A shows detail of EL turn-on period and the current charging spike. The delay time, t_d, is the delay between the application of the voltage pulse (corresponding to the onset of the current spike) and the onset of EL ($t_d \sim 35$ ns). Inset A also shows the fast rise time, $t_1 \sim 60$ ns. The main figure shows the second and slower rise time in the EL, $t_2 \sim 50$ μs. Inset B shows the detail of EL at turn-off on a logarithmic scale. The structure of PFO is also shown.

100 μs 16 V pulses. These figures all show a fast initial rise followed by a slower rise, fast modulation in the turn-off, and a long-lived exponential tail. The delay in EL turn-on, t_d, is hard to discern for device A at the high voltage (41 V) necessary to achieve current densities of order 1 mA cm^{-2}. Similarly, at 41 V the fast rise time recorded by the PMT for device A is ~ 20 ns, and is therefore likely to be limited by the overall response of the system (15–20 ns). For device D at 16 V $t_d \sim 35$ ns, $t_1 \sim 60$ ns (inset A of Fig. 8) and $t_2 \sim 50$ μs. At voltage turn-off the EL drops to $\sim 1/40$ of its previous value (inset B of Fig. 8) and then exponentially decays with $t_4 \sim 25$ μs. Also partly shown in Fig. 7 is the EL spike present on the downward slope of the fast EL modulation (~ 100 ns after voltage turn-off). A spike is also seen for device D ~ 65 ns after voltage turn-off (Fig. 5).

The current spikes seen at the turn-on and turn-off of the voltage pulse are due to the charging and discharging of the device. In the case of device A (see Fig. 7) the capacitance, C, of the device was calculated from the integrated charge, $Q \sim 1.1 \times 10^{-8}$ C, at 41 V to be 260 pF (using $C = Q/V$). This compares to 120 pF calculated for the geometric capacitance of the device [assuming $\epsilon_r = 3$ and using $C = \epsilon_0 \epsilon_r A/L$, where A is the device area (1 nm^2) and L is the device thickness (220 nm)]. Comparison of the integrated charge for the two spikes of device A shows that the initial spike contains a 0.05 A component of quasi-dc current, equal to the magnitude of the quasi-dc current in the device after charging. This implies that dc current is present during device charging. Close inspection of the charging spike reveals that the real rise/fall times of charging (recorded as ~ 10–15 ns) are probably limited by the apparatus rise/fall times (~ 10–15 ns), and therefore that the charging process is much faster than recorded (as would be expected for a capacitor). For further discussion see Ref. 52.

C. Calculation of temperature rise during a pulse

As previously discussed, the presence of significant Joule heating in a device causes the current to increase with

time. In attempting to analyze the temporal response of the LED in terms of the charge carrier dynamics we must, therefore, first ensure that the heating is not significantly contributing to the observed transient responses. We can calculate the temperature rise in the device due to the application of an electrical voltage pulse by referring to the equivalent heat circuit of the device as previously discussed in Ref. 6. To first order, the power dissipated within the device due to Joule heating causes the temperature to rise linearly with time throughout the duration of the pulse. Using the evaporated contact thicknesses for device C (200 nm of calcium, capped with 250 nm of aluminum), the temperature rise per unit time, per unit of power dissipated is calculated to be $\sim 3 \times 10^{-4}$ K (μs)$^{-1}$ (mW)$^{-1}$. This translates to a maximum temperature rise, ΔT_{max} of 0.4 K in the case of device C for a 5 V 0.05 mA pulse of 5 ms. In addition to this we note that the current does not rise significantly over the duration of the pulse, and that both the current and light flatten off to a steady value. We may therefore say, for this particular case, that the heating effects are unlikely to be a major contribution to the slower rise time of EL, t_2. Care must be taken, however, when interpreting t_2 with pulses of higher power to ensure that ΔT_{max} is not the dominant contributor to the rising EL. The presence of a final steady state rather than a continuously increasing current serves as a good diagnostic that Joule heating effects are negligible. For the cases where ΔT_{max} is not expected to be significant, however, the presence of a rising current prior to the final steady state, is likely to be attributable to changing injection conditions rather than heating.

IV. PHENOMENOLOGICAL MODEL

A. The model

Having established our experimental method we now describe the framework within which we interpret these results. In the following we provide a theoretical analysis of the properties of polymer LEDs. The method used relies heavily on models developed for inorganic semiconductors, such that the unique properties of organic polymers enter only into the expression for the field and temperature dependence of the mobility. The microscopic morphology (e.g., disorder) is not fully accounted for, neither for the transport nor for the injection processes. With this limitation in mind, we consider our model to be phenomenological and aim only to establish guidelines for the interpretation of our measurements. We start by writing the equations that are considered to govern the operation of an electrically pumped LED, assuming that the exciton generation is a Langevin process[22,45,40,38]

$$\mu_h = \mu_{h,0} \exp\left(-\frac{\Delta}{kT}\right) \exp(\gamma \sqrt{E}) \tag{7}$$

$$\frac{\partial}{\partial t} n_e(z,t) = \frac{\partial}{\partial z}\left[D_e \frac{\partial}{\partial z} n_e(z,t) + \mu_e(E) n_e(z,t) E(z,t) \right]$$
$$- R_e(z,t) n_e(z,t) \tag{8a}$$

$$\frac{\partial}{\partial t}n_h(z,t)=\frac{\partial}{\partial z}\left[D_h\frac{\partial}{\partial z}n_h(z,t)-\mu_h(E)n_h(z,t)E(z,t)\right]$$
$$-R_h(z,t)n_h(z,t) \qquad (8b)$$

$$\frac{d}{dz}E=\frac{q}{\epsilon}[n_h(z)-n_e(z)] \qquad (9)$$

$$\frac{\partial}{\partial t}S(z,t)=FR_e(z,t)n_e(z,t)+\frac{\partial}{\partial z}\left[D_s\frac{\partial}{\partial z}S(z,t)\right]-\frac{S}{\tau} \qquad (10)$$

$$R_e=\frac{q}{\epsilon_{r>}\epsilon_0}\mu_{\text{eff}}n_h. \qquad (11)$$

Here n_e, n_h, and S are the electron, hole, and singlet exciton density, respectively. D_e and D_h are the electron and hole diffusion coefficients, which are given by $D_e=\mu_e kT/e$ and $D_h=\mu_h kT/e$ (where e is the unit of electrical charge) assuming that the Einstein diffusion relation holds for these systems. z is the distance from the cathode, μ_{eff} is the effective mobility (for $\mu_h\gg\mu_e$ $\mu_{\text{eff}}\equiv\mu_h$), and R_e is the Langevin recombination rate for electrons, which is field dependent through the field dependence of the mobility.[45] Note that the Langevin recombination rate for holes, R_h, and electrons are related through $R_h\times n_h=R_e\times n_e$. The diffusion coefficient for the excitons is derived assuming a diffusion length of $L_D\approx 10$ nm[46] and a lifetime of $\tau=1$ ns ($D_S=L_D^2/\tau$). For simplicity we do not account for nonradiative channels introduced by defects, charges, or other excitons which will shorten the lifetime and may even change the monomolecular nature of the decay.

Equations (8a) and (8b) describe the electron and hole dynamics respectively, whilst Eq. (9) is the Poisson equation. Equation (10) describes the dynamics of the singlet exciton density, which is generated through the Langevin recombination rate [Eq. (11)]. F is the fraction of singlet excitons generated (we assume that F follows the spins statistics argument, $F=1/4$), and τ is the exciton lifetime (not to be mistaken for the radiative lifetime).

B. Boundary conditions

The boundary conditions for the charge carriers are calculated using thermionic emission (including back flow, but ignoring tunneling) as outlined in Ref. 30. We write down the equations for one carrier type (holes) at the anode ($z=L$)

$$n_{h,\text{eqml}}[E(L)]=N_0\exp\left(-\frac{\Delta_b}{kT}\right) \qquad (12)$$

$$J_h=v[n_h(L)-n_{h,\text{eqml}}[E(L)]] \qquad (13)$$

$$v=\frac{AT^2}{N_0} \qquad (14)$$

$$\Delta_b=\Delta_h-e\sqrt{\frac{e|E(L)|}{\epsilon_r}}, \qquad (15)$$

where $n_{h,\text{eqml}}[E(L)]$ is the quasi-equilibrium hole density at the anode, N_0 is the density of conjugated chain segments,
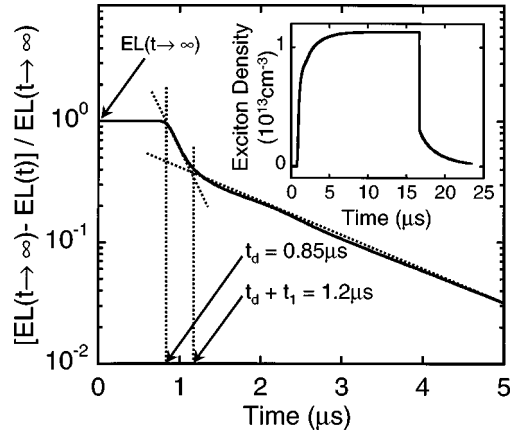

FIG. 9. Plot of the simulated final magnitude of the (normalized) EL minus the EL at time t, $[\text{EL}(t\rightarrow\infty)-\text{EL}(t)]/\text{EL}(t\rightarrow\infty)$, as a function of time density for a PPV-like device (similar to device C), showing how t_d and t_1 are determined. The assumptions used for this simulation are listed in Table II, col. 2. The inset shows the simulated response of the exciton density for a PPV-like device (similar to device C) to a square voltage pulse ($V-V_{\text{bi}}=5$ V). The assumptions used for this simulation are listed in Table II, col. 2.

$1/v$ is the time constant associated with the time it takes to establish equilibrium in the vicinity of the polymer/anode interface, and A is the Richardson constant. Δ_b is the interfacial energy barrier, which is lowered from the zero field value, Δ_h, by the image force effect. There are three more analogous sets of equations describing the hole current at the cathode and the electron currents at both electrodes. The four sets of equations thus formed define the boundary conditions. For the excitons we assume infinitely fast recombination at the contact interface. The extended effect of the contact through coupling of the radiation field to plasmon modes is not included.[47,48] The boundary conditions at time ($t=0$) are derived by solving the equations for $V-V_{\text{bi}}=-V_{\text{bi}}$ at steady state. Such boundary conditions are shown in the inset to Fig. 10 which demonstrates how the polymer is partially filled ("doped") with carriers even for zero applied bias ($V=0$).

C. Parameters used in the model

The values of the parameters used in the modeling work for a PPV-like polymer and a PFO-like polymer device are listed in Table II. The mobility parameters, $\mu_{h,0}$, B, T_0, and γ, for a PPV-like polymer were taken from Ref. 9, and we additionally assume that $\mu_e=0.1\mu_h$.

D. Simulation results

The inset to Fig. 9 shows the response of the average exciton density to a square voltage pulse ($V-V_{\text{bi}}=5$ V). The parameters used correspond to an ITO/PPV-like polymer/Ca device, which in the context of our model corresponds to ohmic contacts. We notice the same features as were experimentally observed, namely: at turn-on, a delay followed by a fast and slow rise, at turn-off, an instantaneous decay, followed by an exponential decay. The same type of response was calculated for various contact barriers and applied voltages. We focus first on the turn-on dynamics and plot the

TABLE III. Definitions of characteristic times t_d, t_1, and t_2. The curve shown here is from the phenomenological model.

Time	Definition
t_d	Time at which the straight line drawn through the first slope on the plot of $\log_e\{[\mathrm{EL}(t\to\infty)-\mathrm{EL}(t)]/\mathrm{EL}(t\to\infty)\}$ vs time intersects with the horizontal section of the curve (i.e., when $[\mathrm{EL}(t\to\infty)-\mathrm{EL}(t)]/\mathrm{EL}(t\to\infty)=1$).
t_d+t_1	Time at which the straight lines drawn through the first and second slopes intersect on the plot of $\log_e[\mathrm{EL}(t\to\infty)-\mathrm{EL}(t)]$ vs time.
t_2	Time at which the EL intensity reaches 95% of its final value (i.e., when $[\mathrm{EL}(t\to\infty)-\mathrm{EL}(t)]/\mathrm{EL}(t\to\infty)=0.05$).
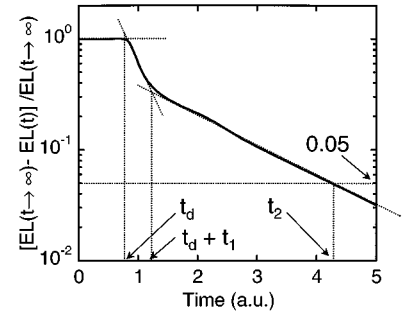
magnitude of the EL at time t, EL(t) shown in the inset of Fig. 9, subtracted from its final value, EL$(t\to\infty)$, i.e., EL$(t\to\infty)-$EL(t), as shown in Fig. 9. This plot clearly reveals the presence of two distinct regions where $\log_e[\mathrm{EL}(t\to\infty)-\mathrm{EL}(t)]$ varies linearly with time. As we show later these two regions are associated with the hole and electron dynamics, which are clearly resolved here due to the assumed order of magnitude difference in mobility, and which can be described by the two time constants, t_1 and t_2. The characteristic times t_d, t_d+t_1 and t_2 are obtained from the plots of $\log_e[\mathrm{EL}(t\to\infty)-\mathrm{EL}(t)]$ versus time and EL versus time as described by Table III.

We wish to find a characteristic time in the device response, which will define the fast carrier (hole) mobility. To do this we plot the hole and electron density adjacent to the electron injecting contact for several time delays. We have chosen the time delays, based on Fig. 9, as $t=t_d=0.85\ \mu$s, $t=t_d+t_1=1.2\ \mu$s, $t=1.7\ \mu$s and steady-state conditions ($t\gg t_2$). Figure 10 shows that at time delays beyond $t=t_d+t_1$ the profile of the hole density is almost constant, with only the electron density still moving into the device. Using
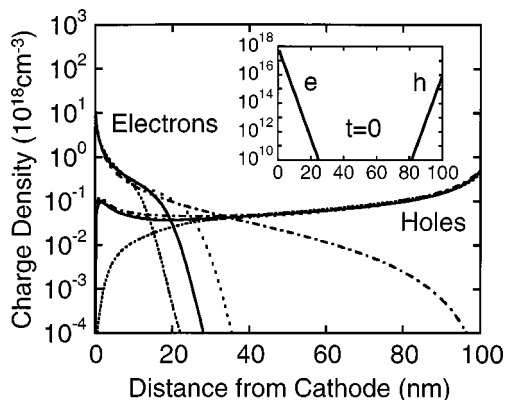

FIG. 10. Simulated electron and hole charge densities as a function of the distance from the cathode density for a PPV-like device (similar to device C) for the times $t=t_d=0.85\ \mu$s (dashed line), $t=t_d+t_1=1.2\ \mu$s (solid line), $t=1.7\ \mu$s (dashed line with large spacings) and for steady-state conditions ($t\gg t_2$) (dashed-dotted line). The inset describes the boundary conditions at $t=0$.

this observation we associate the second time constant (slope) in Fig. 9 with the motion of the slow carriers (electrons). Figure 10 also shows that before $t=t_d+t_1$, the hole density distribution is not yet at its quasistationary state, and that at $t=t_d$ it is still changing relatively fast. It has been discussed by several authors[9,32–34,49] that the determination of mobility values is sensitive to the method used, and in Ref. 9 it was shown that the analysis of t_d from pulsed measurements does not give agreement with the mobility values extracted from the CW $J-V$ characteristics. Since our simulations suggest that only after $t=t_d+t_1$ does the hole density becomes quasistationary, we conclude that the use of $t=t_d+t_1$ is more appropriate than using $t=t_d$ if the deduced mobility is to be compared with other LED characteristics. We find that this method is somewhat similar to the distinction for TOF measurements made between the arrival of the broadened front of the carrier packet and the arrival of the packet's central part. In this context we note that since our simulations do not take account of electrical field-induced broadening found in disordered structures,[50] t_1 is relatively small compared to t_d+t_1.

Using the methodology developed for the TOF technique[50] we examine the ratio $[0.5t_1/(t_d+0.5t_1)]$ which is found here to be equal to ~0.17 at 5 V. This is similar but somewhat larger than the 0.1 deduced from the expression $(2\ kT/eV)^{1/2}$ described in Ref. 50 for an ideal case under constant electric field. Our simulated system is not ideal in the sense that there is a space charge (varying field) and a field-dependent mobility. As we will show, real devices are even less ideal, and this ratio is larger still. We also note that for our method to hold, one must observe the two slopes (time constants) in the experimental turn-on dynamics. If the first time constant is not resolved, due for example to a more extended quenching zone, it is not possible to unambiguously determine the mobility of the fast carriers, as has been discussed in.[32,51] In the experimental curve this will manifest itself when $t_1\gg t_d$ or $(0.5t_1/(t_d+0.5t_1))\approx1$.

We have repeated the simulation for a configuration similar to the PFO device (see Table II) where there is a large imbalance in electron-hole mobility and injection bar-
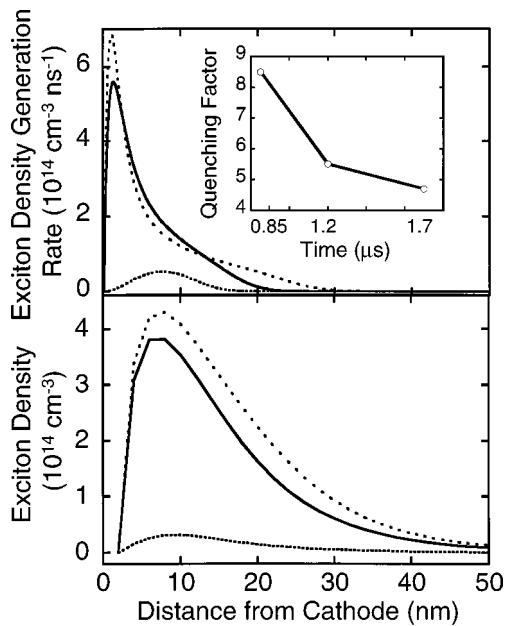
FIG. 11. Calculated distribution of exciton density. (a) The density generated through electron-hole recombination. (b) The same as in (a) but including the effect of excition diffusion and quenching at the electrode interface. The inset shows the factor by which the exciton density is quenched by the interface, as a function of time.

FIG. 12. Calculated electric field distribution for four different points in time. (1) $t=t_{ON}$, just after the applied pulse and before the build up of space charge. (2) $t=t_d+t_1=1.2\ \mu$s holes propagated through the structure, (3) $t=t_{ss}$ is at quasisteady state where space charge is due to both electrons and holes. (4) $t=t_{OFF}$ just after voltage is turned off and only the field is only internal (including space charge).

riers. The shape described in Fig. 9 was reproduced allowing reliable determination of the hole mobility. We also found that the large hole barrier results in low light levels (at low voltages), such that it may be experimentally difficult to resolve the arrival of holes (t_1). The three orders of magnitude lower electron mobility effectively mean that no electrons are injected within the transit time of the holes. Since we do not assume the structure to be empty at $t=0$ (see boundary conditions) there will always be electrons to recombine with the arriving front of the hole distribution. However, this may sometimes be too weak to detect. The signature of this effect may be found in $[0.5t_1/(t_d+0.5t_1)]$ which is significantly larger than the one calculated earlier for the PPV-like device, at the same applied voltage.

The determination of the electron transit time from the EL turn-on is a more complicated process than it is for holes. The motion of electrons into the device gradually increases the overlap of the electron density profile with the hole density profile, giving rise to an increase of the EL intensity. The EL in the electron dominated region therefore does not necessarily follow a single exponential law. Moreover, the distance across which the electrons travel is not as uniquely defined as for the holes (see Figs. 10 and 11). The penetration distance of the electrons, L_e, is limited by recombination with holes, and hence, depends on the actual densities within a given device. The lower limit for this distance would be the size of the quenching zone, L_{qz}, and the upper limit would be the length of the device, L. To be consistent with the deduction of hole mobility the electron transit time needs to be defined as the point where this overlap is close to its maximum value (i.e., steady state). To avoid any ambiguities we define it as the point the EL reaches 0.95 of its final value. Varying this value by ± 0.02 results in only a factor of
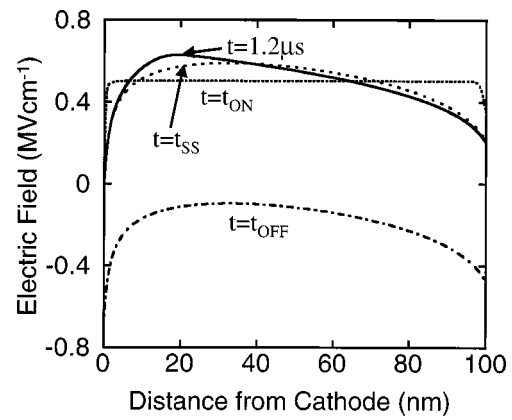
two difference to the electron transit time. We will return to these two sources of error when calculating the electron mobility in PFO (Sec. VI B).

To illustrate the role of the exciton-quenching interface and the electron penetration depth, L_e, we plot, in Fig. 11, the distribution of the exciton density. Figure 11(a) shows the exciton distribution neglecting the diffusion term in Eq. (10), and hence, reflects the distribution of charge recombination rate. Figure 11(b) describes the effect introduced by exciton diffusion and quenching at the electrode (note the different y axis). The times for which those quantities are plotted are consistent with previous figures. The difference between the distribution in the two subfigures demonstrates the effect due to quenching at the interface. We also note that when holes start to arrive at the cathode ($t=t_d$) there is already substantial electron density outside the quenched region so that a non-negligible density of excitons is generated (light can be detected). By calculating the integral under the different curves we can calculate the factor by which the exciton density is reduced due to quenching. This is shown in the inset to Fig. 11 where we note that at longer times the quenching becomes less pronounced, due to the motion of electrons away from the quenching cathode.

For the mobility calculations one also needs to know the electric field throughout the device. A value of $E=(V-V_{bi})/L$ is normally used, which is based on the assumption that the carrier front is not affected by the space charge it is creating. Our simulations show that, since the space charge is created mainly by holes next to the anode, the front of the hole space charge density propagates within a field which increases with time (when the space charge is mainly due to holes). This effect is illustrated in Fig. 12 where the electric field distribution is plotted for $t\sim 0$ (no space charge), $t=t_d+t_1$ (mainly hole induced space charge), $t=t_{ss}$ (steady state, which includes both electron and hole space charge plus a small mutual cancellation). Also shown in this figure is the field distribution when the pulse is turned off and $V-V_{bi}=-V_{bi}$: we come back to this distribution in the text later. For the present discussion we only note that the maxi-

TABLE IV. Summary of the experimental procedure for extracting carrier mobilities including the checks necessary to exclude extraneous effects.

	Experimental check	Reason
1	Avoid impurities associated with oxygen, water or others. Use inert glove box and/or place devices for a long time under vacuum.	Traps or dopants may be introduced and make the intrinsic properties inaccessible.
2	Construct simple heat circuit and make sure $\Delta T < 1$ K for the given pulse width, voltage, current.	Device characteristics are temperature dependent.
3	Avoid interfacial (current blocking) layers next to electrodes (Al_2O_3 for Al electrode will affect hole dynamics, and PEDOT:PSS on ITO will affect electron dynamics).	To ensure the measured quantity is charge transport and not charge accumulation (at interfaces) (see Ref. 4).
4	Ohmic contacts usually involve less ambiguities.	(1) If the injected density is field dependent then, it may be significantly affected by the injection of the other carrier type. (2) If the injected density is low it may be difficult to detect emission due to only the arriving front of the distribution. A large dynamic range in the detection becomes an essential but not necessarily a satisfactory condition.
5	When measuring very slow-carrier mobility, reduce the current due to the fast carrier (i.e., a high barrier). Note the effect on the extraction of the fast carrier mobility (4 earlier).	To ensure that the required long pulse will not result in a temperature rise which in turn will enhance the mobility.
6	Check the frequency dependence of light intensity and operate below the threshold frequency.	Avoid pulse to pulse interference through charge accumulation.
7	Identify the regimes denoted t_d, t_1, t_2, and quasisteady state.	To ensure that the two carrier dynamics are separable.
8	If in doubt regarding 4, a large t_1/t_d ratio (>10) may be indicative of a problem.	If the dynamics of the two carriers intermix through 4, then the apparent t_1 will increase significantly.

mum value of the field does not increase significantly in such a device. This implies that by calculating the mobility using $E = (V - V_{bi})/L$ may result in only a slight overestimation.

E. Additional EL features after turn-off

The turn-off dynamics have been discussed in Ref. 38 where the instantaneous decay was found to be associated with the instantaneous reduction of the internal field in the device as the voltage is turned off, and not to fast carrier extraction.[38] This is illustrated in Fig. 12 for $t = t_{OFF}$. A reduced field, in the bulk, results in a lower mobility, and hence, a reduced exciton generation rate. The following exponential decay is due to the extraction of carriers through the respective contacts. Further experimental results and analysis of the turn-off dynamics will be published elsewhere.[52] We find that in some device configurations two additional features may appear (not necessarily together). The first is a positive spike in the light as the voltage is turned off, and is associated with the increase of the absolute value of the field next to the electrode (see Fig. 12). The second is a delayed bump or a satellite which has the form of a delayed EL feature. The two features are generally associated with high electron density near the cathode, and a quenching zone that is of thickness ≤ 10 nm. In our simulations the high electron density is achieved by using a low energy barriers at the cathode/polymer interface, but we expect that similar effects will be caused by electrons accumu-

lated in trap-like states. The first effect of high electron density is to create a space charge density next to the cathode and hence a reduced field at the recombination zone. When the applied voltage is removed, the field due to the space charge is still present, resulting in an increase in the magnitude of the electric field next to the cathode. Using the same logic as for the instantaneous drop,[38] we can expect a spike to be generated very close to the cathode. The second effect of a high electron density near the cathode is to pull holes towards it (see Fig. 10) and to have a relatively high hole density in the exciton quenching region. When the voltage is turned off and the internal field changes direction, this excess density is pulled away from the quenching zone resulting in a satellite in the light response. This is somewhat similar to the mechanism proposed by Ref. 53 for double layer devices.

V. USE OF METHOD: DETERMINATION OF MOBILITIES

We now apply our mobility determination technique to two devices made of two very different polymers (PPV and PFO). The steps and checks involved in the experimental procedure are highlighted in Table IV. Again we emphasize that we use a sufficiently low repetition rate, 10 Hz for device C and 0.1 Hz for device D. We now consider the variation of the transient behavior of the LEDs with voltage in an attempt to determine the transport properties as a function of the electric field. Figure 13 shows the magnitude of the
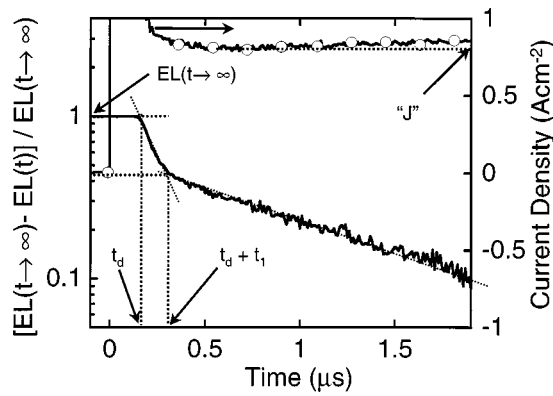
FIG. 13. Plot of the final magnitude of the (normalized) EL minus the EL at time t, $[EL(t\to\infty)-EL(t)]/EL(t\to\infty)$, and the current density as a function of time for device C under 10 V 2 μs pulses with 10 Hz repetition frequency. J denotes the current density for the mobility calculated from the SCLC theory.

(normalized) EL subtracted from its long-time value, $[EL(t\to\infty)-EL(t)]/EL(t\to\infty)$ for device C in response to 10 V 2 μs pulses using a 10 Hz repetition frequency. The figure shows how the method used to deduce t_d and t_1 from the modeled data (as shown in Fig. 9) can be applied to deduce t_d and t_1 from the experimental data. Linear variations of $\log_e\{[EL(t\to\infty)-EL(t)]/EL(t\to\infty)\}$ versus time, t, are observed, and these give the periods t_1 and t_2, as was found from the phenomenological model (Fig. 9).

A. PPV copolymer mobility

Figure 14 shows qualitatively how t_d and t_1 vary as a function of applied voltage for device C, which, as previously discussed, is not injection limited in this voltage range. Note the differences in time scale of the responses at 3 (inset) and 16 V. The data has been normalized to the value of the EL at the transition between the first and second rise times, $EL(t=t_d+t_1)$, and shows that the initial rise time decreases sharply with increasing voltage. It is interesting to note (i) that t_d and t_1 decrease by three to four orders of magnitude over the given field range, and (ii) that the ratio of $0.5t_1$ to $(t_d+0.5t_1)$ is a function of voltage (inset to Fig. 15).
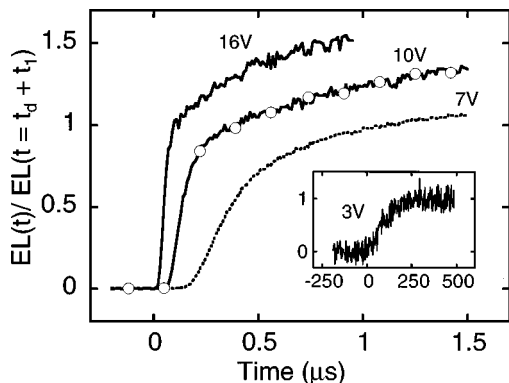
FIG. 14. EL response of device C as a function of time for different applied voltages (7, 10, and 16 V) showing the behavior of t_d and t_1. The electric field has been normalized to its value at $t=t_d+t_1$. The inset shows the EL response of the device to 3 V pulses for comparison.
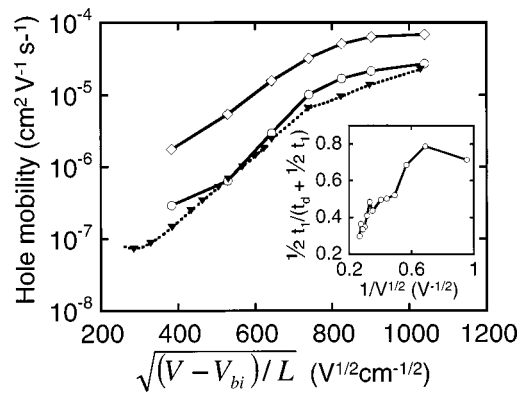
FIG. 15. Calculated hole mobility as a function of the square root of the electric field for device C using different definitions of the carrier transit time, t_T, and the electric field, E, in the device: $t_T=t_d$, $E_{int}=V/L$ (open diamonds); $t_T=t_d+t_1$, $E_{int}=V/L$ (open circles). Also shown is the mobility calculated from the SCLC theory (filled triangles) from the current density vs voltage data in pulsed mode (see Fig. 3). The inset shows (t_1/t_d+t_1) as a function of the square root of the electric field.

This ratio is indicative of the degree of broadening of the hole packet in the device, and its value (~0.5 at $V-V_{bi}=5$ V) is found to be larger than that deduced from our simulations (0.17 at $V-V_{bi}=5$ V). This may be due to the disorder and field-induced broadening discussed in Ref. 50.

We now calculate hole mobility from the t_d and t_1 data from device C. Figure 15 shows the hole mobility as a function of the square root of the internal electric field calculated for device C by three different methods. These methods can be summarized by the following three equations:

$$\mu_1=\frac{L^2}{(V-V_{bi})t_d}$$

$$\mu_2=\frac{L^2}{(V-V_{bi})(t_d+t_1)} \tag{16}$$

$$\mu_3=\frac{8}{9}\frac{JL^3}{\epsilon_0\epsilon_r(V-V_{bi})^2}, \tag{17}$$

where V_{bi} is the built-in voltage in the device which is assumed, from the difference between the workfunctions of ITO and Ca, to be 1.9 V for devices C and D. μ_1 is calculated from t_d alone and does not take into account the variation of the electric field across the device due to the space charge. μ_2 is calculated from t_d+t_1, and uses the same average electric field as used for μ_1. Finally, μ_3 is calculated entirely independently of t_d and t_1 by using the quasisteady-state current density, J, and rearranging the SCLC equation [Eq. (2)] to give the mobility.

From Fig. 15 we see that the hole mobility, μ_1, calculated from t_d alone result in mobility values that are approximately one order of magnitude higher than those predicted by SCLC theory (μ_3). This is in contrast to the good agreement we see between the mobility deduced using $t_d+t_1(\mu_2)$ and the hole mobility, μ_3, calculated using the $J-V$ data and Eq. (17) for space charge limited conduction. This agreement implies (i), that the method presented to determine the hole mobility from transient data is reliable, (ii) that the device is dominated by SCLC over this field range, and (iii) that our assumption that the doped PEDOT layer

acts as an injection contact is valid. The actual shape of the curve is also of interest. At fields below ~ 0.65 MV cm^{-1}, corresponding to $[(V-V_{bi})/L]^{1/2}=800$ V$^{1/2}$ cm$^{-1/2}$, the logarithm of the hole mobility increases with voltage and is approximately proportional to the square root of the electric field as has been measured before.[22,31,54–56] In this field regime we can therefore describe the hole mobility by

$$\mu_h = \mu_{h,0} \exp\left(-\frac{\Delta}{kT}\right) \exp(\gamma_h \sqrt{E}) \tag{18}$$

from which we find that $\mu_{h,0}\exp(-\Delta/kT)=3.5 \times 10^{-9}$ cm^2 V^{-1} s^{-1} and $\gamma_h = 1.0 \times 10^{-2}$ cm$^{1/2}$ V$^{-1/2}$. We also attempted to use the longer time-scale transient data to determine the electron mobility for the PPV copolymer as a function of voltage, from the values of t_2. This proved possible for applied voltages of 3–5 V, from which electron mobilities of $\sim 5 \times 10^{-9} - 1 \times 10^{-8}$ cm^2 V^{-1} s^{-1} were obtained. These values for corresponding voltages are found to be ~ 100 times less than the calculated hole mobility. (This compares to the value of ~ 10 that was used in the model, which represents the lower limit such that the hole and electron motions can be separately time resolved). For this device, however, it was not possible to use this method at significantly higher voltages due to the current-induced heating effects, as discussed earlier. For example, at 10 V the current is seen to increase before the EL has reached steady state. This in turn causes the EL to increase, making the determination of t_2 impossible. For a 1 ms 10 V pulse, the device current is ~ 1000 mA cm^{-2} and the temperature rise is calculated to be ~ 5 K. The method of obtaining the electron mobility from values of t_2 is therefore limited to low voltages for high current density devices (within the present heat-sinking scheme). We should also note that in this devices structure the PEDOT layer may also be serving as an electron blocking layer thus making the measured electron dynamics a mixture of electron transport and electron accumulation due to that interface.

B. PFO mobility

As a final demonstration of our method we analyze the parameters for the PFO polymer which was recently characterized using a TOF technique.[24] As discussed earlier, device D/(ITO/PFO/Ca) is hole-injection limited, so we expect the density of electrons in the device to be much greater than that for holes. It is still likely, however, that $\mu_h \gg \mu_e$, and therefore that once injected, the holes will quickly move across the device, and that the device is space-charge limited with respect to electrons. The hole mobility can therefore be extracted from t_1 data just as for device C (see discussion in the phenomenological-model section). Due to the predominance of the low mobility electrons compared to the higher mobility holes, we therefore find that significantly less current flows in device D than in device C. For a given voltage, the Joule heating effects are thus considerably reduced in device D. Device D therefore represents an ideal system for obtaining the electron mobility from t_2 data using the following equation:
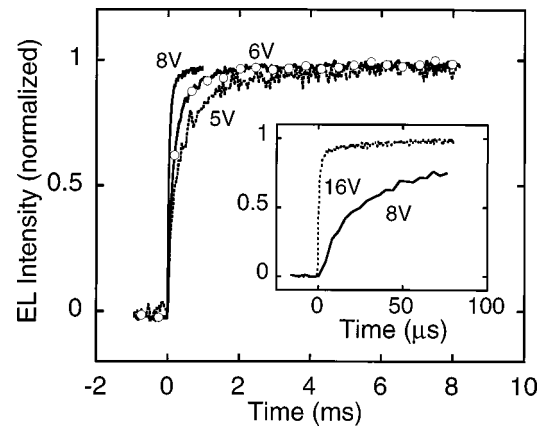

FIG. 16. EL response of device D as a function of time for different applied voltages (5, 6, and 8 V), showing the behavior of t_2. The inset shows the EL response of the device to 8 and 16 V pulses for comparison. The electric field has been normalized to its final magnitude.

$$\mu_e = \frac{L_e L}{(V-V_{bi})t_2}, \tag{19}$$

where t_2 is defined here as the time at which the magnitude of the EL reaches 0.95 (of its final value (see Sec. IV C). L is the device thickness and L_e is the penetration distance of the electrons into the device (see Sec. IV C). As L_e could vary from the thickness of the quenching zone (~ 20 nm) to the total thickness of the device (100 nm), the electron mobility could be up to five times smaller than it would be assuming that electrons penetrate the entire thickness of the device (i.e. $L_e = L$). Figure 16 shows the longer EL time response of device D to pulses of 5, 6, and 8 V to illustrate how t_2 changes with voltage. The inset compares the response of the device to 8 and 16 V pulses (note the differing time scales of the figure and the inset). For example, at 5 V $t_2 \sim 5$ ms, whereas at 16 V $t_2 \sim 50$ μs. By referring back to Fig. 8 we may also compare the values of (t_1+t_d) to t_2 at 16 V, from which we see that the ratio of $(t_1+t_d):t_2$ at 16 V is ~ 450. This same ratio will apply to the values to be calculated for the hole and electron mobilities. The maximum temperature rise during the 80 μs 16 V pulse, with 0.06 A, was determined to be ~ 0.5 K.

Figure 17 shows the hole mobility for device D, calculated using Eq. (16) from the t_1+t_d data, the electron mobility using Eq. (19) calculated from the t_2 data, and the mobility calculated using Eq. (17) assuming a SCLC model. When analyzing the transient data for holes in the PFO device one needs to consider the effect of the high energy barrier for hole injection. The processes governing charge injection for nonohmic contacts are not entirely clear and hence may influence the apparent transit time of the holes (see Table IV). The large mobility mismatch ($\mu_h \sim 1000 \times \mu_e$) and the fact that the holes are injection limited, makes the determination of the hole mobility difficult at low voltages due to quenching (as discussed in Sec. V B). We have therefore separated the hole mobilities calculated for the lowest two voltages (for which $t_1/t_d \sim 20$) from the other values.
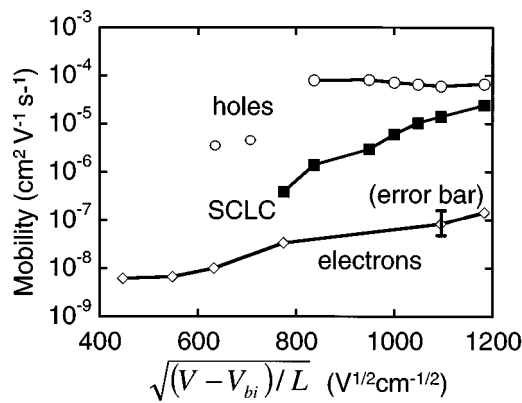
FIG. 17. Calculated carrier mobility as a function of the square root of the electric field for device D: hole mobility calculated from $t_T = t_d + t_1$, $E_{int} = V/L$ (open circles); electron mobility calculated from $t_T = t_2$, $E_{int} = V/L$ (open diamonds) and an average carrier mobility calculated from the SCLC theory (filled squares). Also shown on the electron mobility curve is an error bar to illustrate the errors in both the electron penetration depth and transit time.

The determination of the electron mobility, however, is legitimate since the electron-injecting contact is ohmic. We know, however, that there are two sources of error associated in determining the electron mobility from the experimental data, namely the electron penetration depth, L_e, and the electron's characteristic transit time, t_2. It is also true that the electric field is nonuniform in the vicinity of the cathode. As has been previously described, the range of values for the electron's penetration depth is $20 \, nm \leqslant L_e \leqslant 100 \, nm$. Similarly the error in t_2 results from the nonexponential nature of the EL in the electron dominated region (see Sec. IV C). The sum of these errors results in a nonlinear error bar (~ 5 times higher and ~ 2 times lower) and is plotted on one point in Fig. 17 by means of illustration. The error in determining the hole mobility is smaller than the error for electron mobility as it suffers from neither of the two principal error sources encountered for electrons, as discussed earlier. The hole mobility of PFO is also found to be less field dependent in the high field regime than for the PPV copolymer. In addition, the values calculated are found to be roughly consistent with those derived from TOF measurements.[24] The electron mobility (calculated from t_2) is found to be ~ 3 orders of magnitude lower than the hole mobility for a given field. We also note that the logarithm of the electron mobility increases linearly with the square root of the internal electric field as described by

$$\mu_e = \mu_{e,0} \exp\left(-\frac{\Delta'}{kT} \right) \exp\left(\gamma_e \sqrt{E} \right) \qquad (20)$$

from which we find that $\mu_{e,0} \exp(-\Delta'/kT) = 7.5 \times 10^{-10} \, cm^2 \, V^{-1} \, s^{-1}$ and $\gamma_e = 4.4 \times 10^{-3} \, cm^{1/2} \, V^{-1/2}$.

The mobility calculated from the SCLC theory alone cannot be fitted to either the electron or hole mobility calculated from the transient data. This is probably due to the current both electron and hole components: the holes are injection limited and the electrons are space-charge limited. The mobility calculated from the SCLC theory may be considered to be an ''average'' mobility of both electrons and holes. At low fields the SCLC mobility tends to the lower electron mobility suggesting that the current is significantly contributed to by electrons, whilst at high fields holes are likely to dominate.

VI. SUMMARY AND CONCLUSIONS

We have presented detailed analysis of pulsed excitation in polymer LEDs. Our analysis is based on universal features found in various device configurations and based on either PPV or PFO, polymers which are both different and important. We find that, as in the case for TOF measurements, the method of extracting the mobility is very important. Using numerical simulations we have devised a method which is consistent both with CW drive of LEDs and probably also with the TOF technique. We have also shown that the interplay of electrons and holes needs to be accounted for, and showed that mobility values for both types of carriers can be determined using a single device. Finally, we have shown that mobility values can also be determined for device structures that do not lend themselves to CW analysis (e.g., the ITO/PFO/Ca device).

ACKNOWLEDGMENTS

[1] S. Karg, V. Dyakonov, M. Meier, W. Riess, and G. Paasch, Synth. Met. **67**, 165 (1994).
[2] D. Braun, D. Moses, C. Zhang, and A. J. Heeger, Appl. Phys. Lett. **61**, 3092 (1992).
[3] H. Vestweber, R. Sander, A. Greiner, W. Heitz, R. F. Mahrt, and H. Bässler, Synth. Met. **64**, 141 (1994).
[4] J. Pommerehne, H. Vestweber, Y. H. Tak, and H. Bässler, Synth. Met. **76**, 67 (1996).
[5] D. R. Baigent, P. G. May, and R. H. Friend, Synth. Met. **76**, 149 (1996).
[6] N. Tessler, N. T. Harrison, D. S. Thomas, and R. H. Friend, Appl. Phys. Lett. **73**, 732 (1998).
[7] N. Tessler, N. T. Harrison, and R. H. Friend, Adv. Mater. **10**, 64 (1998).
[8] H. Chayet, R. Pogreb, and D. Davidov, Phys. Rev. B **56**, 12702 (1997).
[9] P. W. M. Blom and M. C. J. M. Vissenberg, Phys. Rev. Lett. **80**, 3819 (1998).
[10] V. G. Kozlov, P. E. Burrows, G. Parthasarathy, and S. R. Forrest, Appl. Phys. Lett. **74**, 1057 (1999).
[11] J. C. Sturm, W. Wilson, and M. Iodice, IEEE J. Sel. Top. Quantum Electron. **4**, 75 (1998).
[12] D. J. Pinner, N. Tessler, and R. H. Friend, Synth. Met. **102**, 1108 (1999).
[13] N. T. Harrison, N. Tessler, C. J. Moss, K. Pichler, and R. H. Friend, Opt. Mater. **9**, 178 (1998).
[14] J. S. Kim, M. Granstrom, R. H. Friend, N. Johansson, W. R. Salaneck, R. Daik, W. J. Feast, and F. Cacialli, J. Appl. Phys. **84**, 6859 (1998).
[15] S. A. Carter, M. Angelopoulos, S. Karg, P. J. Brock, and J. C. Scott, Appl. Phys. Lett. **70**, 2067 (1997).
[16] J. C. Carter *et al.*, Appl. Phys. Lett. **71**, 34 (1997).
[17] S. Karg, M. Meier, and W. Riess, J. Appl. Phys. **82**, 1951 (1997).
[18] M. Meier, S. Karg, K. Zuleeg, W. Brutting, and M. Schwoerer, J. Appl. Phys. **84**, 87 (1998).
[19] T. Kugler, M. Logdlund, and W. R. Salaneck, IEEE J. Sel. Top. Quantum Electron. **4**, 14 (1998).
[20] A. C. Arias, M. Granstrom, D. S. Thomas, K. Petrisch, and R. H. Friend, Phys. Rev. B **60**, 1854 (1999).
[21] N. C. Greenham and R. H. Friend, in *Solid State Physics*, edited by H. Ehrenreich and F. A. Spaepen (Academic, New York, 1995), Vol. 49, pp. 2–150.

[22] P. W. M. Blom and M. J. M. de Jong, IEEE J. Sel. Top. Quantum Electron. **4**, 105 (1998).

[23] CT-GP/A current probe, Bergoz Instrumentation (1998).

[24] M. Redecker and D. D. C. Bradley, Appl. Phys. Lett. **73**, 1565 (1998).

[25] R. C. Weast, *Handbook of Chemistry and Physics* (Chemical Rubber Corp., Boca Raton, FL, 1978).

[26] V. I. Arkhipov, E. V. Emelianova, Y. H. Tak, and H. Bässler, J. Appl. Phys. **84**, 848 (1998).

[27] H. Ishii, K. Sugiyama, D. Yoshimura, E. Ito, Y. Ouchi, and K. Seki, IEEE J. Sel. Top. Quantum Electron. **4**, 24 (1998).

[28] I. G. Hill, A. Rajagopal, and A. Kahn, Appl. Phys. Lett. **73**, 662 (1998).

[29] I. H. Campbell, P. S. Davids, D. L. Smith, N. N. Barashkov, and J. P. Ferraris, Appl. Phys. Lett. **72**, 1863 (1998).

[30] P. S. Davids, I. H. Campbell, and D. L. Smith, J. Appl. Phys. **82**, 6319 (1997).

[31] M. van der Auweraer, F. C. de Schryver, P. M. Borsenberger, and H. Bassler, Adv. Mater. **6**, 199 (1994).

[32] L. Pautmeier, R. Richert, and H. Bässler, Philos. Mag. B **63**, 587 (1991).

[33] P. M. Borsenberger, E. H. Magin, M. van der Auweraer, and F. C. de Schryver, Phys. Status Solidi A **140**, 9 (1993).

[34] M. Abkowitz, H. Bässler, and M. Stolka, Philos. Mag. B **63**, 201 (1991).

[35] P. W. M. Blom, M. J. M. de Jong, and M. G. van Munster, Phys. Rev. B **55**, R656 (1997).

[36] P. W. M. Blom, M. J. M. de Jong, and S. Breedijk, Appl. Phys. Lett. **71**, 930 (1997).

[37] A. J. Campbell, M. S. Weaver, D. G. Lidzey, and D. D. C. Bradley, J. Appl. Phys. **84**, 6737 (1998).

[38] N. Tessler, D. J. Pinner, V. Cleave, D. S. Thomas, G. Yahioglu, P. Lebarny, and R. H. Friend, Appl. Phys. Lett. **74**, 2764 (1999).

[39] N. F. Mott and R. W. Gurney, *Electronic Processes in Ionic Crystals* (Oxford University Press, London, 1940).

[40] G. G. Malliaras, and J. C. Scott, J. Appl. Phys. **85**, 7426 (1999).

[41] N. Tessler, Adv. Mater. **11**, 363 (1999).

[42] A. J. Campbell, D. D. C. Bradley, and D. G. Lidzey, Opt. Mater. **9**, 114 (1998).

[43] A. J. Campbell, D. D. C. Bradley, and D. G. Lidzey, J. Appl. Phys. **82**, 6326 (1997).

[44] R. Osterbacka, A. J. Pal, K. M. Kallman, and H. Stubb, J. Appl. Phys. **83**, 1748 (1998).

[45] U. Albrecht and H. Bässler, Phys. Status Solidi B **191**, 455 (1995).

[46] J. J. M. Halls, K. Pichler, R. H. Friend, S. C. Moratti, and A. B. Holmes, Appl. Phys. Lett. **68**, 3120 (1996).

[47] R. M. Amos and W. L. Barnes, Phys. Rev. B **55**, 7249 (1997).

[48] H. Becker, S. E. Burns, and R. H. Friend, Phys. Rev. B **56**, 1893 (1997).

[49] H. Scher and E. Montroll, Phys. Rev. B **12**, 2455 (1975).

[50] R. Richert, L. Pautmeier, and H. Bässler, Phys. Rev. Lett. **63**, 547 (1989).

[51] V. R. Nikitenko, Y. H. Tak, and H. Bässler, J. Appl. Phys. **84**, 2334 (1998).

[52] D. J. Pinner, R. H. Friend, and N. Tessler, Appl. Phys. Lett. (submitted).

[53] V. R. Nikitenko, V. I. Arkhipov, Y. H. Tak, J. Pommerhene, and H. Bässler, J. Appl. Phys. **81**, 7514 (1997).

[54] L. B. Schein, A. Peled, and D. Glatz, J. Appl. Phys. **66**, 686 (1989).

[55] A. Ioannidis, E. Forsythe, Y. Gao, M. W. Wu, and E. M. Conwell, Appl. Phys. Lett. **72**, 3038 (1998).

[56] E. M. Conwell and M. W. Wu, Appl. Phys. Lett. **70**, 1867 (1997).

[57] S. M. Sze, *Physics of Semiconductor Devices*, 2nd ed. (Wiley, New York, 1981).